

# Super-Expansion of Assembled Reduced Graphene Oxide Interlayers by Segregation of Al Nanoparticle Pillars for High-Capacity Na-Ion Battery Anodes

SeongJi Pyo,<sup>#</sup> Wonsik Eom,<sup>#</sup> You Jin Kim, Sang Hoon Lee, Tae Hee Han,<sup>\*</sup> and Won-Hee Ryu<sup>\*</sup>

Cite This: *ACS Appl. Mater. Interfaces* 2020, 12, 23781–23788

Read Online

ACCESS |

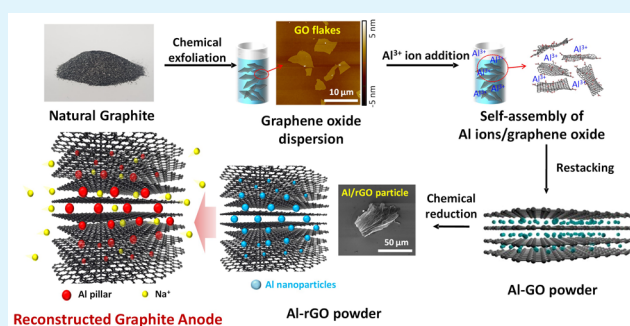
Metrics & More

Article Recommendations

Supporting Information

**ABSTRACT:** The applicability of Na-ion batteries is contingent on breakthroughs in alternative electrode materials that have high capacities and which are economically viable. Unfortunately, conventional graphite anodes for Li-ion battery systems do not allow Na-ion accommodation into their interlayer space owing to the large ionic radius and low stabilizing energy of Na in graphite. Here, we suggest a promising strategy for significantly increasing Na capacity by expanding the axial slab space of graphite. We successfully synthesized reconstructed graphite materials via self-assembly of negative graphene oxide (GO) flakes and Al cation (positive) pillars and by subsequent chemical reaction of the obtained Al-GO materials. Al pillars, atomically distributed in graphite interlayers, can extend the slab space by up to  $\sim 7$  Å, which is a 2-fold interlayer distance of pristine graphite. An exceptionally high capacity of 780 mAh/g is demonstrated for reconstructed graphite anodes with Al pillars, compared with rGO materials (210 mAh/g). We investigated the electrochemical reaction mechanism and structural changes associated with discharge and charge to emphasize the benefit of using reconstructed graphite as anodes in Na-ion batteries. Our strategy of modifying the interlayer distance by introducing metallic pillars between the layers can help address the low capacity of carbonaceous anodes.

**KEYWORDS:** reconstructed graphite, anode, Na ion battery, metallic pillar, reduced graphene oxide



## INTRODUCTION

Ensuring the economy of rechargeable batteries has become a considerably challenging issue given the rising costs and shortage of raw materials associated with modern lithium ion (Li-ion) batteries.<sup>1,2</sup> The localized nature of Li deposits, especially in South America, increases concerns about the supply of Li, which negatively affects the cost of the batteries.<sup>3</sup> Sodium ion (Na-ion) batteries are a promising option for low-cost rechargeable batteries.<sup>4–7</sup> The similarity of electrode materials and cell structure across Li- and Na-ion batteries has great practical potential.<sup>8,9</sup>

Recent trends in the Na-ion battery development have been focused on suitable electrode materials, because larger Na ions (1.02 Å) often exhibit low capacity and sluggish intercalation kinetics, compared with Li ions (0.76 Å).<sup>9,10</sup> In addition, the low stability of Na accommodation sites for conventional electrode materials reduces available capacity and intercalation kinetics.<sup>11</sup> For example, graphite-based anodes for Li-ion batteries do not demonstrate sufficient capacity in Na-ion cells.<sup>12</sup> In this regard, hard carbons, which comprise a class of nongraphitic carbon materials, have been utilized for better Na intercalation reaction.<sup>13–15</sup> Extra pores and enlarged space around non-stacking graphene layers in the hard carbon can accommodate more Na ions and enable facile surface absorption of Na ions

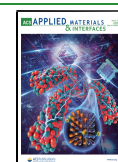
into the pores, increasing the capacity up to 300 mAh/g.<sup>16</sup> However, the high material cost of hard carbons and their structural instability associated with the short-range-ordered carbon stacking structure should be addressed for developing proper carbon anode alternatives. Na ions are inserted at a low potential near 0 V related to the Na electrodeposition on hard carbons, which could lead to serious safety concerns during fast charging.<sup>17</sup>

An interesting approach, expanding the slab space of graphite materials instead of using non-graphitic carbons, has been considered by Wang's group.<sup>18</sup> Functionalized anion species on graphene layers and their self-stacking for reduction can form expanded graphite and increase the interlayer distance up to 4.3 Å compared with  $\sim 3.4$  Å for pristine graphite. The manipulated graphite materials can yield a high capacity of up to 284 mAh/g and stable cyclability, even for high current densities.<sup>18</sup> Graphite

Received: January 20, 2020

Accepted: May 4, 2020

Published: May 4, 2020



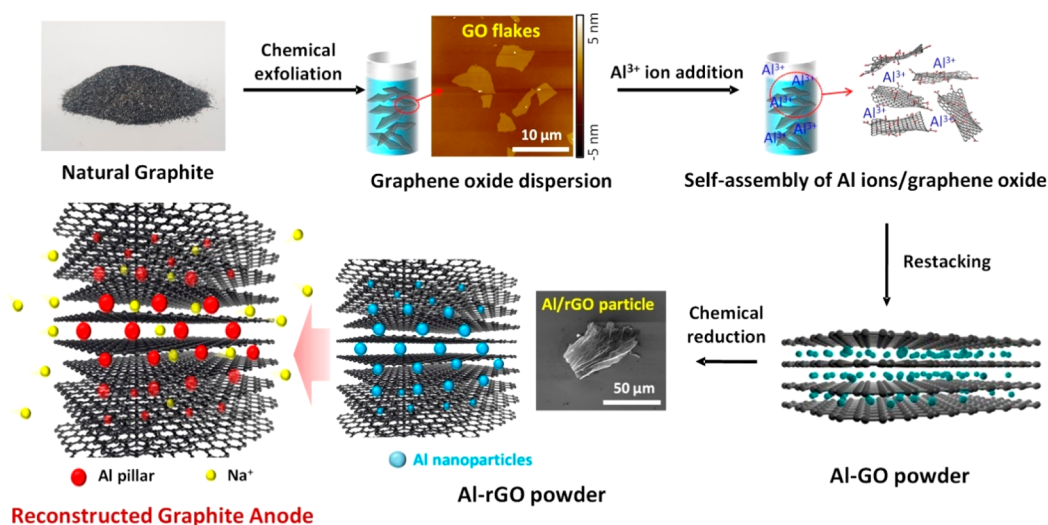


**Figure 1.** Concept map of controlling the interlayer space and synthesis of reconstructed graphite. Schematic of steps for obtaining reconstructed graphite anode materials for Na-ion batteries using Al pillars. Negatively charged graphene oxide flakes are self-assembled with  $\text{Al}^{3+}$  cations. After the chemical reduction step, interlayer expansion can be achieved by introducing atomically distributed Al pillars between the graphite layers.

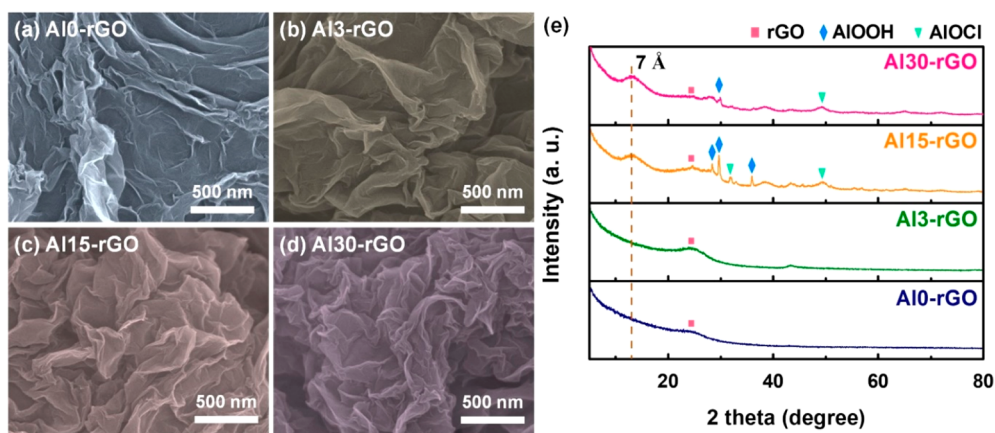


**Figure 2.** Morphological features and crystalline information on the reconstructed  $\text{Al}_x$ -rGO materials. SEM images of the reconstructed graphite materials ( $\text{Al}_x$ -rGO) with different amounts of Al pillar species: (a)  $\text{Al}_0$ -rGO, (b)  $\text{Al}_3$ -rGO, (c)  $\text{Al}_{15}$ -rGO, and (d)  $\text{Al}_{30}$ -rGO. (e) XRD patterns of the reconstructed graphite materials ( $\text{Al}_x$ -rGO), for different amounts of Al pillar species. The XRD peak near  $12.6^\circ$  in the small-angle region shows the expanded slab space ( $\sim 7$  Å) between the graphite interlayers.

reconstruction can be performed by inserting oxygen species via oxidation and the subsequent reduction of graphite materials, which is known as the Hummers' method; this approach allows consistent expansion of the slab spacing along the  $c$ -axis.<sup>19</sup> The interlayer space and the consequent available capacity correspond to the types and number of functionalized anion species (e.g., epoxide and hydroxyl).<sup>19–21</sup> Although efforts have been made to develop reconstructed graphite using reduced graphene oxide (rGO) obtained using the Hummers' method, most approaches manipulated anion species functionalized on graphene.<sup>22,23</sup> The negatively charged surface of rGO sheets by anion functional species means that a repulsive force can be restacked among the rGO layers, which consequently hinders large interlayer space expansion and the long-range stacking of rGO materials.<sup>24–26</sup> In addition, many oxygen anion species between reconstructed graphite layers can easily react with Na ions, forming irreversible sodium oxide byproducts, similar to the solid electrolyte interphase (SEI) layer.<sup>27,28</sup> Therefore, introducing proper pillar ions between rGO layers could be a suitable solution for the further improvement of reconstructed graphite anodes. Controlling the interlayer distance and further

expanding the slab space may allow for easy accommodation of a number of large Na ions corresponding to the higher capacity value.

In this study, we suggest a facile and effective way of synthesizing extremely reconstructed graphite anode materials for Na-ion batteries, by employing  $\text{Al}^{3+}$  cation pillar ions (Figure 1). Negatively charged graphene oxide (GO) layers can be self-assembled owing to the electrostatic attractive interaction with positively charged  $\text{Al}^{3+}$  ions in the dispersing solution of GO sheets. Repeated self-assembly of negative(GO)–positive( $\text{Al}^{3+}$  ions)–negative(GO) enables long-range-ordered structures of GO layers and enhances the structural and mechanical stability of reconstructed graphite materials. We controlled the interlayer distance of rGO by using different concentrations of the Al pillar ion species in the GO dispersed solution. We evaluated the electrochemical performance of the reconstructed graphite anodes for different Al pillar amounts. Our synthetic strategy of expanding the graphite interlayer by metallic pillars provides a novel direction for development of graphitic carbon anode materials for Na-ion batteries.

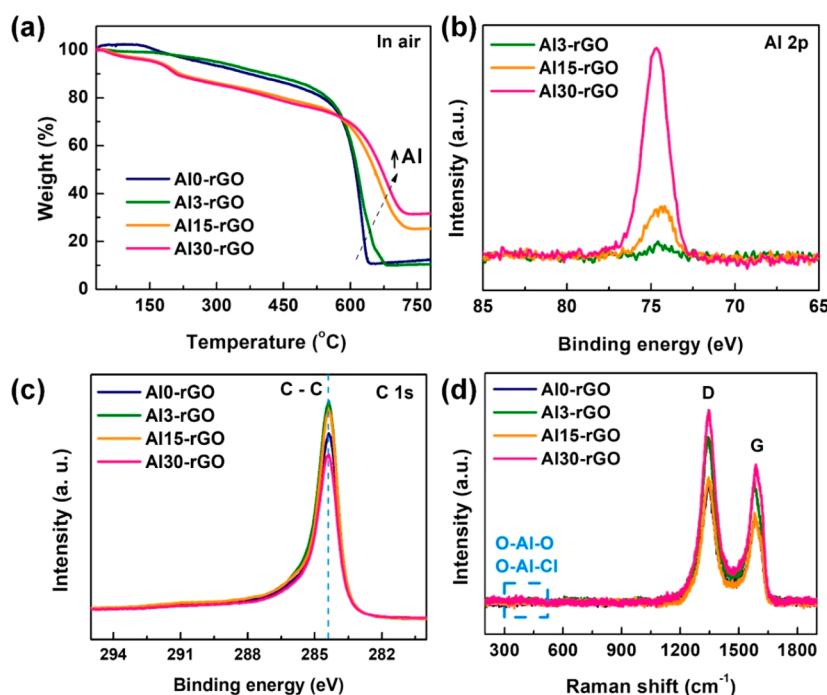


**Figure 3.** Chemical composition and bonding properties of the synthesized  $\text{Al}_x\text{-rGO}$  materials. (a) TGA curves of the graphite materials ( $\text{Al}_x\text{-rGO}$ ) reconstructed with different amounts of Al pillar species. XPS results for the  $\text{Al}_3\text{-rGO}$ ,  $\text{Al}_{15}\text{-rGO}$ , and  $\text{Al}_{30}\text{-rGO}$  for (b) Al 2p and (c) C 1s. (d) Raman spectra of the reconstructed graphite materials ( $\text{Al}_x\text{-rGO}$ ) with different amounts of Al pillar species.

To fabricate reconstructed graphite materials, pristine graphite was oxidized and subsequently exfoliated to prepare a dispersed GO solution as a precursor (Figure 1).  $\text{AlCl}_3$  solution was mixed with the prepared GO dispersed solution, to obtain self-stacking structures between  $\text{Al}^{3+}$  ions and negatively charged GO sheets.<sup>29</sup> The obtained Al-embedded GO powder (Al-GO) was chemically reduced to obtain Al-intercalated rGO materials (Al-rGO or  $\text{Al}_x\text{-rGO}$ ). According to the different concentrations of the  $\text{AlCl}_3$  solution, sample names were simply classified as  $\text{Al}_0\text{-rGO}$  (pristine rGO),  $\text{Al}_3\text{-rGO}$ ,  $\text{Al}_{15}\text{-rGO}$ , and  $\text{Al}_{30}\text{-rGO}$ , respectively. To investigate the effect of the Al addition on the morphologies of the obtained Al-rGOs, scanning electron microscopy (SEM) images of samples were acquired; these are shown in Figure 2a–d. No significant nucleation and/or segregation of Al particles on the studied rGO sheets was observed, indicating that the atomic Al species are properly inserted between the sheets as a pillar component. We observed that the extent of wrinkles on the rGO sheets increased with increasing amounts of added Al. This suggests self-assembly by the electrostatic attraction between  $\text{Al}^{3+}$  cations and negatively charged GO sheets. X-ray diffraction (XRD) analysis was performed to examine the crystalline structure and lattice distance of the obtained Al-rGOs (Figure 2e). Using the Bragg law ( $2d \sin \theta = n\lambda$ , where  $d$  is the interplanar spacing,  $\theta$  is the scattering angle,  $\lambda$  is the wavelength, and  $n$  is an integer quantifying the reflection order), we determined the lattice distance in the (002) plane in the reconstructed graphite materials.<sup>30</sup> For pristine rGO ( $\text{Al}_0\text{-rGO}$ ), a broad peak near  $24^\circ$  indicated an aligned interlayer ( $\sim 3.8 \text{ \AA}$ ) along the  $c$ -axis of the reconstructed graphite. Interestingly, an additional peak appeared at a smaller angle of  $12.6^\circ$ , corresponding to the long lattice distance of  $\sim 7 \text{ \AA}$  with increasing the amount of the added  $\text{Al}^{3+}$  species ( $\text{Al}_{15}\text{-rGO}$  and  $\text{Al}_{30}\text{-rGO}$ ). The results demonstrate that high amounts of Al pillar species can extensively expand the lattice distance between (002) planes.

During the chemical reduction process of the Al-GO powder,  $\text{Al}^{3+}$  ions were also reduced to Al-containing nanoparticles (i.e.,  $\text{AlOOH}$  and  $\text{AlOCl}$ ) because  $\text{Al}^{3+}$  species in the GO dispersion existed as solvated ions surrounded by  $\text{H}_2\text{O}$  molecules. Comparing the peak broadness of the reconstructed graphite layers and Al-containing particles, the former exhibited broader peaks, suggesting that the peak for the smaller angle of  $12.6^\circ$  is mainly associated with the expansion of graphene layers by the Al pillar components. The reconstructed graphite layers could allow large Na ions to be efficiently accommodated during discharge.

Thermogravimetric analysis (TGA) was performed by increasing temperature under normal atmospheric conditions to investigate the thermal decomposition mechanism and to estimate the Al contents in the Al-rGO materials (Figure 3a). All of the analyzed Al-rGO samples exhibited a sudden weight loss near  $550 \text{ }^\circ\text{C}$ , owing to the carbon decomposition into carbon mono- and/or dioxide gases by reacting with oxygen gases. The residual weight of Al-rGOs increased with increasing amounts of the Al precursor solution, corresponding to a fraction of the Al pillar species in the reconstructed graphite. The atomic contents of  $\text{Al}_x\text{-rGO}$  were presented in Table S1. The residual weight values of  $\text{Al}_0\text{-rGO}$ s and  $\text{Al}_3\text{-rGO}$ s were almost the same, at 10 wt %. However, the end edge of the decomposition region for the Al-containing sample was shifted toward higher temperatures, over  $650 \text{ }^\circ\text{C}$ , which was attributed to the formation of aluminum oxides ( $\text{Al}_2\text{O}_3$ ). This trend was also observed for samples with higher Al contents ( $\text{Al}_{15}\text{-rGO}$  and  $\text{Al}_{30}\text{-rGO}$ ). X-ray photoelectron spectroscopy (XPS) measurements were carried out to examine the surface composition and structure of  $\text{Al}_x\text{-rGO}$  samples (Figure S1). To further confirm the existence of Al pillars in the analyzed samples, Figure 3b shows the XPS measurements for the  $\text{Al}_3\text{-rGO}$ ,  $\text{Al}_{15}\text{-rGO}$ , and  $\text{Al}_{30}\text{-rGO}$  samples, collected in the Al 2p region, respectively. The peak intensity increased with increasing the amount of Al added to

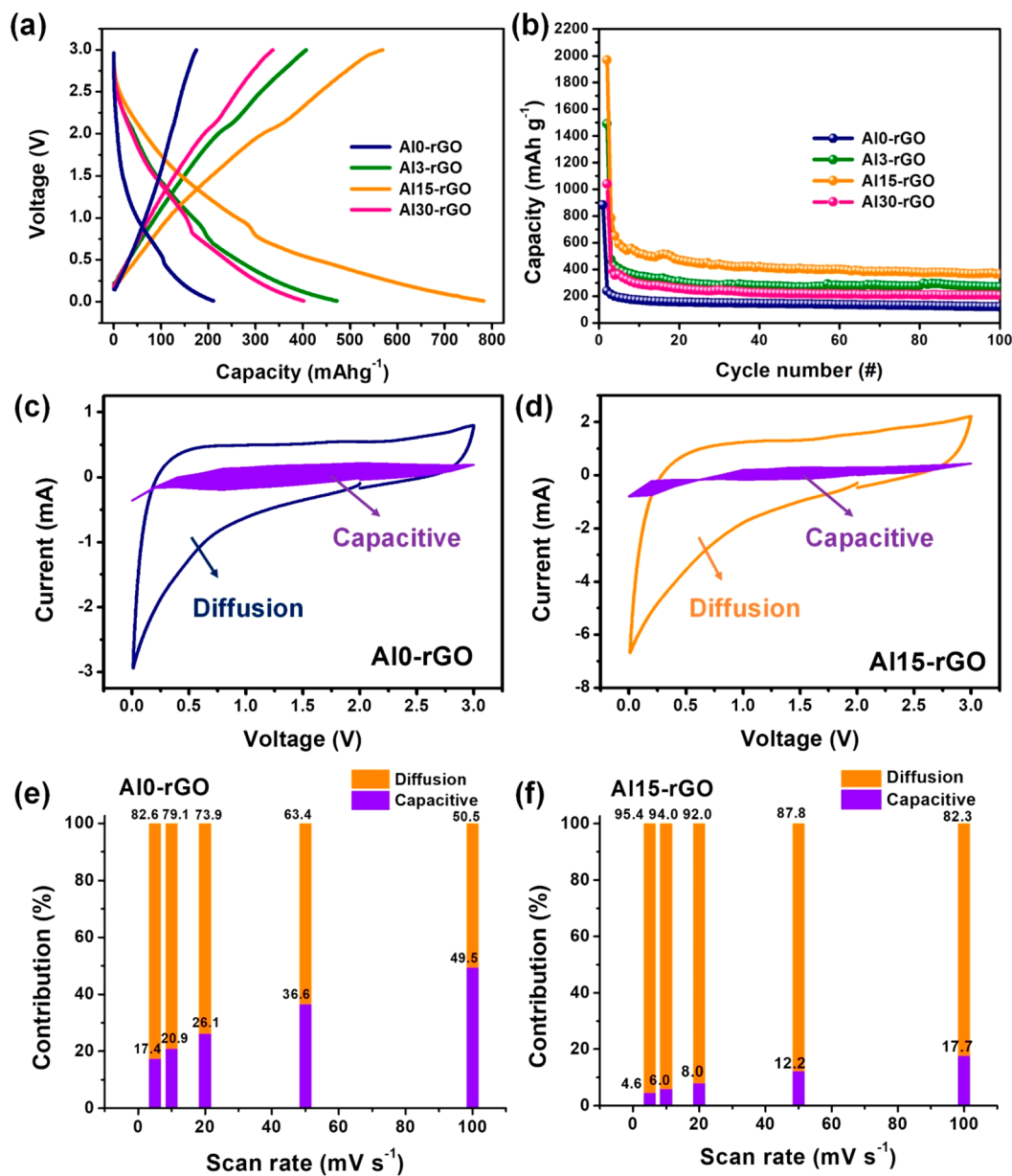


**Figure 4.** Properties of electrochemical cells with  $\text{Al}_x\text{-rGO}$  anode materials. (a) Second charge/discharge curves and (b) cycle performance of Na-ion cells with the reconstructed graphite anode materials ( $\text{Al}_x\text{-rGO}$ ) with different amounts of Al pillar species, for voltage in the 0.01–3 V range, for a current density of  $50 \text{ mA g}^{-1}$ . Cyclic voltammograms of (c)  $\text{Al}_0\text{-rGO}$  and (d)  $\text{Al}_{15}\text{-rGO}$  with capacitive and diffusion contributions, at a scan rate of  $10 \text{ mV/s}$ . Fractional contributions for (e)  $\text{Al}_0\text{-rGO}$  and (f)  $\text{Al}_{15}\text{-rGO}$ , for electrochemical reactions at different scan rates.

the samples. The peak attributed to the Al pillar at  $\sim 74.6 \text{ eV}$  was observed for all samples, indicating the existence of the  $\text{AlOOH}$  species.<sup>31,32</sup> The peak analysis of XPS spectra were shown in Figure S2. The Al 2p spectra were split into Al–Cl ( $75.1 \text{ eV}$ ) and Al–OH ( $74.2 \text{ eV}$ ), and each of these signifies the content of  $\text{AlOCl}$  and  $\text{AlOOH}$ , respectively. Depending on the amount of added Al precursor, the content ratio of Al–Cl and Al–OH was changed. In detail, the content of Al–OH ( $62.3\%$ ) was higher than that of Al–Cl ( $37.7\%$ ) in  $\text{Al}_{15}\text{-rGO}$ , presented in Figure S2c. These results were consistent with XRD results (Figure 2e), where the peak intensity of Al–OOH was stronger for  $\text{Al}_{15}\text{-rGO}$  than that for  $\text{Al}_{30}\text{-rGO}$ . It is noted that  $\text{AlOOH}$  contributes to the battery performance over  $\text{AlOCl}$ , considering that  $\text{Al}_{15}\text{-rGO}$  has better battery performance than  $\text{Al}_{30}\text{-rGO}$ . In addition, no O–Al–O and/or O–Al–Cl molecular vibrations in the Raman spectra (Figure S3) in the low

wavelength range ( $300\text{--}500 \text{ cm}^{-1}$ ) were observed, suggesting a uniform distribution of Al-containing nanoparticles between rGO sheets.<sup>33</sup> The extent of the GO reduction in the analyzed samples was determined using XPS (Figures 3c and S4) and Raman spectroscopy (Figures 3d and S3). In the XPS profiles, the strong intensity at  $284.5 \text{ eV}$  of the C–C bond and the signal that gradually declines toward higher binding energies quantify the extent of the GO reduction.<sup>34</sup> GO was chemically reduced by hydrazine, which significantly eliminated C–O functional group, indicating the complete reduction of GO. In addition, when overlapped, the XPS spectra of the  $\text{Al}_x\text{-rGO}$  samples, there is no significant difference between samples. Therefore, it is considered that reduction level among the samples is almost same according to concentration of Al. In Raman spectroscopy, the relative intensity ratio ( $I_D/I_G$ ) between D ( $1345 \text{ cm}^{-1}$ ) and G ( $1585 \text{ cm}^{-1}$ ) peaks is widely used for quantifying the

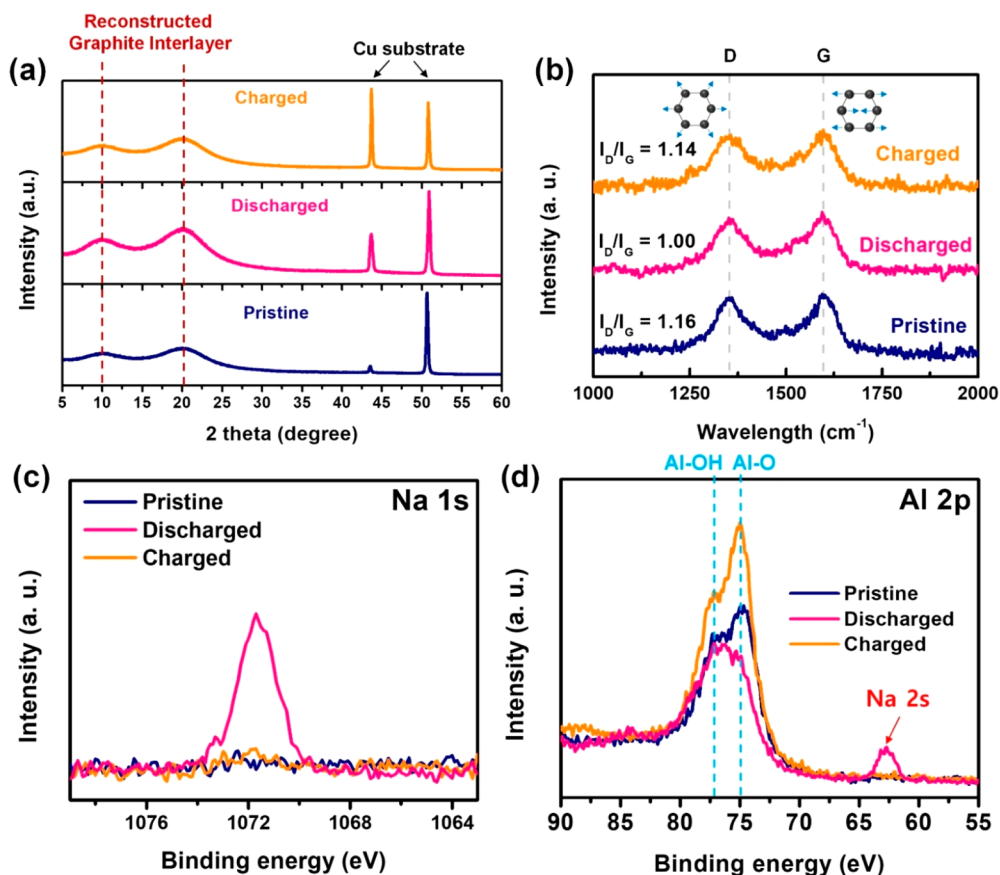


**Figure 5.** Ex situ measurements of Al $x$ -rGO electrodes. (a) Ex situ XRD patterns and (b) Raman spectra for the pristine, discharged, and charged Al15-rGO electrodes. Ex situ XPS for the pristine, discharged, and charged Al15-rGO electrodes, collected for (c) Na 1s and (d) Al 2p.

structural restoration of rGO.<sup>35,36</sup> Because the Al $x$ -rGO samples exhibited similar XPS C 1s spectra and  $I_D/I_G$  ( $\sim 1.16$ ), the reduction extent for the Al $x$ -rGO samples was the same. Analysis of XPS full spectra also confirmed no atomic impurities in the analyzed samples, except the Al pillars. This implies that the Na-ion battery performance (Figure 4) of these prepared materials is only affected by the interlayer space formed by the Al pillars.

The electrochemical performance of Na-ion cells with Al $x$ -rGO electrodes was examined to validate the advantage of expanded interlayer distance supported by Al pillar species (Figure 4a,b). A sloping curve characteristic of the Al $x$ -rGO electrodes without a plateau indicates one-phase reaction because the insertion and extraction of Na<sup>+</sup> into the Al $x$ -rGO electrodes readily occurs due to the enlarged slab spacing (Figure 4a). While pristine rGO (Al0-rGO) exhibited a low capacity of 210 mAh/g at second cycle, Al pillar-incorporated rGO anode materials exhibited significantly higher charge and discharge capacities of Na-ion cells. Al15-rGO exhibited an exceptional discharge capacity of 782 mAh/g, compared with Al3-rGO (472 mAh/g) and Al30-rGO (401 mAh/g). Even the capacity of Al3-rGO, for which there was a negligible amount of Al pillars between rGO layers, was 2-fold higher than that of Al0-rGO. With increasing the Al pillar fraction (Al0-rGO  $\rightarrow$  Al15-rGO), the cell capacity increased up to 780 mAh/g (approximately 2–4 times higher than that of the pristine rGO sample and/or reported values for carbon materials).<sup>13,37–40</sup> Due to the unique morphological features of the Al-rGO materials, the adsorption reaction of Na ions on their pore entrance and extra spaces could be significantly boosted prior to insertion reaction and the numerable Na<sup>+</sup> adsorption

sites on the Al-rGO materials can consequently contribute to increase capacity value above 1 V.<sup>41–43</sup> However, the capacity for Al30-rGO was lower than those for the samples with smaller amounts of Al pillars. Although Al pillars can accommodate more Na ion carriers in the expanded slab space of rGO, a large amount of pillars can block the accommodation sites of Na ions and hinder the movement of Na ions in rGO layers. Therefore, a proper amount of pillar species should be introduced, for maximizing the electrochemical performance of reconstructed graphite. We investigated the cycle performance of the prepared Al-rGO samples (Figures 4b and S5). Irreversible capacity loss was observed after the initial cycle and following cycles, because Na ions extensively reacted with oxygen species in the Al-rGO samples. This is consistent with previous reports on rGO electrode materials.<sup>44,45</sup> This drawback can be addressed by introducing sacrificial additives into the cathode to relieve irreversible capacity or by reducing the fraction of oxygen in Al-rGO.<sup>46,47</sup> Although a substantial fraction of initial capacity is irreversibly lost after an initial discharge, capacity is gradually stabilized during initial cycling and is maintained for 100 cycles with an average Coulombic efficiency of >99% (Figures 4b, S6, and S7). Al15-rGO anode material exhibits the highest capacity of 370 mAh/g after 100 cycles, compared with other analyzed Al-rGO materials. To further elucidate the electrochemical behavior of the analyzed Al-rGO samples, cyclic voltammetry (CV) profiles were computed and are shown in Figure 4c,d. The shapes of the CV curves for all the analyzed Al $x$ -rGO samples are qualitatively similar across different scan rates. Distortion of the rectangular shape in the CV curves indicates Faradaic adsorption and desorption of Na ions with respect to insertion and

extraction of Na<sup>+</sup> for electrochemical reduction and oxidation, respectively.<sup>48</sup> Therefore, the electrochemical reaction of Al-rGO during charging and discharging should be considered as consisting of two parts: (i) Faradaic contribution attributed to the insertion/extraction of Na<sup>+</sup>, including the diffusion of Na ions, and (ii) capacitive contribution attributed to the double-layer capacitance/pseudocapacitance.<sup>49</sup> The current contributions to the CV profile come from the capacitive- and diffusion-controlled currents. Using Dunn's method, a mixture of electrochemical reactions can be described at a specific potential, to estimate the fractional contributions of the capacitive-controlled ( $k_1v$ ) and diffusion-controlled ( $k_2v^{1/2}$ ) processes, using the following equation:

$$i = k_1v + k_2v^{1/2}$$

by calculating  $k_1$  and  $k_2$ , the fractional areas for the two electrochemical processes can be obtained from the CV data (Figures S8 and S9).<sup>48,50</sup> Figure 4c,d shows the CV profiles for the Al0-rGO and Al15-rGO materials, with the separation of two different contributions, collected at 10 mV/s. The values of the corresponding contributions for the diffusion control and capacitive control, for different scan rates, are shown in Figure 4e,f. Interestingly, the diffusion-controlled contribution for the reconstructed graphite sample with Al pillar species (Al15-rGO, 93.0%) was higher than that of the pristine sample without Al pillars (Al0-rGO, 79.1%). This suggests that the expanded interlayer space owing to Al pillars between graphene layers effectively facilitates diffusion of Na ions in these structures. Although the diffusion contribution for the Al0-rGO sample continuously decreased up to 50.5% with increasing the scan rate, the Al15-rGO sample exhibited a relatively high diffusion-controlled contribution (17.7%) even for a high scan rate of 100 mV/s, confirming the facile Na<sup>+</sup> intercalation reaction in the expanded interlayer space supported by Al pillars. The higher number of Na accommodation sites and their facile ion diffusion in the reconstructed graphite with Al pillars significantly improve the electrochemical performance of Na-ion cells. With increasing the Al content in the rGO samples (Al0rGO → Al15-rGO), the diffusion contribution increases. However, for the Al30-rGO sample the diffusion-controlled component becomes smaller, because a very large amount of Al pillars in the Al30-rGO sample probably contributed to blocking Na sites and hindering the Na diffusion. This observation is consistent with charge–discharge results (Figure 4a,b), suggesting that there is an optimal level of pillar species. The improved kinetic properties of Al15-rGO samples compared to pristine rGO (Al0-rGO) also imply the advantage of the assembled rGO materials with Al pillar species as promising anodes for emerging Na-ion batteries (Figure S10).

To confirm the structural advantages of using reconstructed graphite materials with Al pillars, ex situ XRD results for the Al15-rGO electrodes, for different electrochemical states, are presented in Figure 5a. The as-prepared pristine electrode was soaked in the electrolyte, as with the discharged and charged electrodes. In addition to the peaks corresponding to the Cu substrate, two strong peaks at 10 and 20° were observed for the electrode sample, unlike for the powder materials. Subpeaks attributed to AlOOH and AlOCl became weaker owing to the high intensity of main peaks in the reconstructed graphite. This was attributed to the spontaneous insertion of solvent species into the expanded interlayer space, and subsequent rearrangement of the enlarged slab space in the Al15-rGO sample. The main peak was located at a smaller angle of 10°, compared with

the powder sample for which the peak was at 13° (Figures 5a and 2e), indicating that the expanded interlayer space is further expanded owing to the possible introduction of electrolyte species. No peak shifts were observed after discharge and charge, implying that the reconstructed graphite exhibits zero-stain characteristics during the insertion/extraction of large Na ions. Ex situ Raman spectroscopy results are also shown to further explore the structural change in the carbons in the reconstructed graphite, with respect to discharge and charge (Figure 5b). All of the analyzed samples exhibited typical D and G bands, at ~1355 and ~1600 cm<sup>-1</sup>.  $I_D/I_G$  decreased (1.16 → 1.00) after discharge and was reversibly retrieved after charge (1.14). The D band corresponds to the in-plane breathing vibrations of aromatic ring structures ( $A_{1g}$  symmetry), and the G band corresponds to the in-plane stretching vibration of sp<sup>2</sup> carbon ( $E_{2g}$  symmetry), as shown in the inset of Figure 5b.<sup>51</sup> During Na<sup>+</sup> insertion (discharge), hexagonal carbon rings are distorted by occupying interstitial sites, preferentially located at the central side of the carbon ring between the graphite layers. The distorted ring structure is recovered after Na<sup>+</sup> extraction (charge), verifying a reversible intercalation reaction of Na ions to/from the reconstructed graphite electrodes. Reversible intercalation characteristics of Na ions for the reconstructed graphite with Al pillars were further confirmed using ex situ XPS characterization of the pristine, discharged, and charged electrodes in the Na 1s and Al 2p spectral regions, respectively (Figure 5c,d). There were no significant peaks related to the Na component, for the pristine electrode. A strong Na peak appeared after discharge, and its magnitude decreased after reverse charge, implying reversible intercalation reactions for discharge and charge. For the Al 2p spectral region, we also observed an additional peak at ~63 eV, corresponding to Na 2s from the discharged electrode; this peak disappeared after discharge, consistent with XPS profiles observations for Na 1s.<sup>52</sup> Interestingly, we observed notable changes in the Al–OH and Al–O peak magnitudes for electrochemical reactions.<sup>53</sup> The pristine electrode exhibited a weak-magnitude Al–OH peak and a relatively strong Al–O peak. The intensity of the Al–O peak decreased after discharge, and the peak was retrieved after reverse charge. This result demonstrates that oxygen species coordinated with Al can react with Na ions for discharge. Although no crystalline products of Na<sub>2</sub>O were observed, oxygen anions could form oxide products (i.e., amorphous Na<sub>2</sub>O) in a side reaction with the inserted Na ions. Capacity was not proportional to the amount of Al pillars in the reconstructed graphite, meaning that Al pillars are not the main active materials in Na-ion cells (Figure 4a). However, they could partially participate in the discharge reaction, donating oxygen species and subsequently forming sodium oxide species. Nevertheless, the reversibility of the Al–O peak after discharge and charge confirms that the unexpected side reaction regarding oxygen species is reversible and does not deteriorate the electrochemical performance of electrode materials in Na-ion cells. To shed more light on this finding, detailed studies of reconstructed graphite with Al pillars should be performed. Expansion of the graphite interlayer by the introduction of metallic pillar components offers novel synthetic pathways for developing high-capacity carbon materials. Reconstructed graphite can also be utilized as anodes in beyond-Li-ion batteries based on diverse alkali metal ions (e.g., Na, K, Mg, and Al ions).

## CONCLUSION

In summary, we reported a simple and effective route for realizing considerable expansion of the axial slab space between graphite interlayers by introducing trivalent metallic ( $\text{Al}^{3+}$ ) pillars.  $\text{Al}^{3+}$  ions were self-assembled with negatively charged GO flakes dispersed in the aqueous solution, then Al species were atomically distributed as pillars between the rGO interlayers after chemical reduction. The reconstructed graphite anode materials with Al pillar species exhibited an expanded axial interlayer of  $\sim 7 \text{ \AA}$ , thereby facilitating insertion/extraction of large Na ions. The reconstructed graphite anodes demonstrated exceptional capacity, reaching 780 mAh/g, which was almost 4-fold higher than that for the pristine rGO-based anode (210 mAh/g). Optimization of the Al amount in reconstructed graphite should be considered for maximizing the latter's electrochemical performance. We elucidated the electrochemical mechanism in reconstructed graphite in terms of its diffusion-controlled contribution compared to the pristine rGO. Unexpectedly, we also found that oxygen species bound with Al pillars reversibly reacted with Na ions. The studied graphite materials with expanded interlayer space stably maintained their two-dimensional structure without severe expansion and shrinkage during the large Na intercalation reaction, as zero-strain reaction characteristics. Controlling the interlayer distance in graphite materials by the introduction of metallic pillar species suggests an effective method for maximizing the accommodation of large Na ions and for facilitating the movement of Na ions.

## ASSOCIATED CONTENT

### Supporting Information

The Supporting Information is available free of charge at <https://pubs.acs.org/doi/10.1021/acsami.0c00659>.

Experimental procedures, XPS results, Raman spectra results, Coulombic efficiency results, CV and the corresponding electrochemical contribution results, atomic percent of Alx-rGO materials (PDF)

## AUTHOR INFORMATION

### Corresponding Authors

**Tae Hee Han** – Department of Organic and Nano Engineering, Hanyang University, Seoul 04763, Republic of Korea; [orcid.org/0000-0001-5950-7103](https://orcid.org/0000-0001-5950-7103); Email: [than@hanyang.ac.kr](mailto:than@hanyang.ac.kr)

**Won-Hee Ryu** – Department of Chemical and Biological Engineering and Institute of Advanced Materials and Systems, Sookmyung Women's University, Seoul 04310, Republic of Korea; [orcid.org/0000-0002-0203-2992](https://orcid.org/0000-0002-0203-2992); Email: [whryu@sookmyung.ac.kr](mailto:whryu@sookmyung.ac.kr)

### Authors

**Seongji Pyo** – Department of Chemical and Biological Engineering, Sookmyung Women's University, Seoul 04310, Republic of Korea

**Wonsik Eom** – Department of Organic and Nano Engineering, Hanyang University, Seoul 04763, Republic of Korea

**You Jin Kim** – Department of Chemical and Biological Engineering, Sookmyung Women's University, Seoul 04310, Republic of Korea

**Sang Hoon Lee** – Department of Organic and Nano Engineering, Hanyang University, Seoul 04763, Republic of Korea

Complete contact information is available at:

<https://pubs.acs.org/10.1021/acsami.0c00659>

## Author Contributions

#S.P. and W.E. contributed equally to this work.

## Notes

The authors declare no competing financial interest.

## ACKNOWLEDGMENTS

This work was supported by the National Research Foundation of Korea (NRF) grant funded by the Korean government (MSIT) (Nos. 2019R1C1C1007886 and 2019M3D1A2104105). This research was also supported by the Korea Evaluation Institute of Industrial Technology (KEIT) grant funded by the Korean government (MOTIE) (No. 10077594). This work was supported by the National Research Foundation of Korea (NRF) grant funded by the Korean government (MSIT) (No. 2018R1A5A1025224).

## REFERENCES

- (1) Tarascon, J.-M. Is Lithium the New Gold? *Nat. Chem.* **2010**, *2*, 510–510.
- (2) Liu, J.; Bao, Z.; Cui, Y.; Dufek, E. J.; Goodenough, J. B.; Khalifah, P.; Li, Q.; Liaw, B. Y.; Liu, P.; Manthiram, A.; Meng, Y. S.; Subramanian, V. R.; Toney, M. F.; Viswanathan, V. V.; Whittingham, M. S.; Xiao, J.; Xu, W.; Yang, J.; Yang, X.-Q.; Zhang, J.-G. Pathways for Practical High-Energy Long-Cycling Lithium Metal Batteries. *Nature Energy* **2019**, *4*, 180–186.
- (3) Gupta, S. From Gadgets to the Smart Grid. *Nature* **2015**, *526*, S90–S91.
- (4) Xu, X.; Niu, C.; Duan, M.; Wang, X.; Huang, L.; Wang, J.; Pu, L.; Ren, W.; Shi, C.; Meng, J.; Song, B.; Mai, L. Alkaline Earth Metal Vanadates as Sodium-Ion Battery Anodes. *Nat. Commun.* **2017**, *8*, 460.
- (5) Ryu, W.-H.; Wilson, H.; Sohn, S.; Li, J.; Tong, X.; Shaulsky, E.; Schroers, J.; Elimelech, M.; Taylor, A. D. Heterogeneous  $\text{WS}_x/\text{WO}_3$  Thorn-Bush Nanofiber Electrodes for Sodium-Ion Batteries. *ACS Nano* **2016**, *10*, 3257–3266.
- (6) Lim, S.-J.; Han, D.-W.; Nam, D.-H.; Hong, K.-S.; Eom, J.-Y.; Ryu, W.-H.; Kwon, H.-S. Structural Enhancement of  $\text{Na}_3\text{V}_2(\text{PO}_4)_3/\text{C}$  Composite Cathode Materials by Pillar Ion Doping for High Power and Long Cycle Life Sodium-Ion Batteries. *J. Mater. Chem. A* **2014**, *2*, 19623–19632.
- (7) Vaalma, C.; Buchholz, D.; Weil, M.; Passerini, S. A Cost and Resource Analysis of Sodium-Ion Batteries. *Nat. Rev. Mater.* **2018**, *3*, 18013.
- (8) Jung, J.-W.; Ryu, W.-H.; Yu, S.; Kim, C.; Cho, S.-H.; Kim, I.-D. Dimensional Effects of  $\text{MoS}_2$  Nanoplates Embedded in Carbon Nanofibers for Bifunctional Li and Na Insertion and Conversion Reactions. *ACS Appl. Mater. Interfaces* **2016**, *8*, 26758–26768.
- (9) Yabuuchi, N.; Kubota, K.; Dahbi, M.; Komaba, S. Research Development on Sodium-Ion Batteries. *Chem. Rev.* **2014**, *114*, 11636–11682.
- (10) Ryu, W.-H.; Jung, J.-W.; Park, K.; Kim, S.-J.; Kim, I.-D. Vine-like  $\text{MoS}_2$  Anode Materials Self-Assembled from 1-D Nanofibers for High Capacity Sodium Rechargeable Batteries. *Nanoscale* **2014**, *6*, 10975–10981.
- (11) Lee, N.-W.; Jung, J.-W.; Lee, J.-S.; Jang, H.-Y.; Kim, I.-D.; Ryu, W.-H. Facile and Fast Na-Ion Intercalation Employing Amorphous Black  $\text{TiO}_{2-x}/\text{C}$  Composite Nanofiber Anodes. *Electrochim. Acta* **2018**, *263*, 417–425.
- (12) Kundu, D.; Talaie, E.; Duffort, V.; Nazar, L. F. The Emerging Chemistry of Sodium Ion Batteries for Electrochemical Energy Storage. *Angew. Chem., Int. Ed.* **2015**, *54*, 3431–3448.
- (13) Irisarri, E.; Ponrouch, A.; Palacin, M. R. Review—Hard Carbon Negative Electrode Materials for Sodium-Ion Batteries. *J. Electrochem. Soc.* **2015**, *162*, A2476–A2482.
- (14) Komaba, S.; Murata, W.; Ishikawa, T.; Yabuuchi, N.; Ozeki, T.; Nakayama, T.; Ogata, A.; Gotoh, K.; Fujiwara, K. Electrochemical Na

Insertion and Solid Electrolyte Interphase for Hard-Carbon Electrodes and Application to Na-Ion Batteries. *Adv. Funct. Mater.* **2011**, *21*, 3859–3867.

(15) Stevens, D. A.; Dahn, J. R. High Capacity Anode Materials for Rechargeable Sodium-Ion Batteries. *J. Electrochem. Soc.* **2000**, *147*, 1271–1273.

(16) Xiao, B.; Rojo, T.; Li, X. Hard Carbon as Sodium-Ion Battery Anodes: Progress and Challenges. *ChemSusChem* **2019**, *12*, 133–144.

(17) Kang, H.; Liu, Y.; Cao, K.; Zhao, Y.; Jiao, L.; Wang, Y.; Yuan, H. Update on Anode Materials for Na-Ion Batteries. *J. Mater. Chem. A* **2015**, *3*, 17899–17913.

(18) Wen, Y.; He, K.; Zhu, Y.; Han, F.; Xu, Y.; Matsuda, I.; Ishii, Y.; Cumings, J.; Wang, C. Expanded Graphite as Superior Anode for Sodium-Ion Batteries. *Nat. Commun.* **2014**, *5*, 4033.

(19) McAllister, M. J.; Li, J.-L.; Adamson, D. H.; Schniepp, H. C.; Abdala, A. A.; Liu, J.; Herrera-Alonso, M.; Milius, D. L.; Car, R.; Prud'homme, R. K.; Aksay, I. A. Single Sheet Functionalized Graphene by Oxidation and Thermal Expansion of Graphite. *Chem. Mater.* **2007**, *19*, 4396–4404.

(20) Kang, Y.-J.; Jung, S. C.; Choi, J. W.; Han, Y.-K. Important Role of Functional Groups for Sodium Ion Intercalation in Expanded Graphite. *Chem. Mater.* **2015**, *27*, 5402–5406.

(21) Gao, C.; Feng, J.; Dai, J.; Pan, Y.; Zhu, Y.; Wang, W.; Dong, Y.; Cao, L.; Guan, L.; Pan, L.; Hu, H.; Wu, M. Manipulation of Interlayer Spacing and Surface Charge of Carbon Nanosheets for Robust Lithium/Sodium Storage. *Carbon* **2019**, *153*, 372–380.

(22) Cabello, M.; Bai, X.; Chyrka, T.; Ortiz, G. F.; Lavela, P.; Alcántara, R.; Tirado, J. L. On the Reliability of Sodium Co-Intercalation in Expanded Graphite Prepared by Different Methods as Anodes for Sodium-Ion Batteries. *J. Electrochem. Soc.* **2017**, *164*, A3804–A3813.

(23) Xu, Z. L.; Park, J.; Yoon, G.; Kim, H.; Kang, K. Graphitic Carbon Materials for Advanced Sodium-Ion Batteries. *Small Methods* **2019**, *3*, 1800227.

(24) Dong, L.; Chen, Z.; Zhao, X.; Ma, J.; Lin, S.; Li, M.; Bao, Y.; Chu, L.; Leng, K.; Lu, H.; Loh, K. P. A Non-Dispersion Strategy for Large-Scale Production of Ultra-High Concentration Graphene Slurries in Water. *Nat. Commun.* **2018**, *9*, 76.

(25) Smith, R. J.; Lotya, M.; Coleman, J. N. The Importance of Repulsive Potential Barriers for the Dispersion of Graphene using Surfactants. *New J. Phys.* **2010**, *12*, 125008.

(26) Wang, Y.; Wu, Y.; Huang, Y.; Zhang, F.; Yang, X.; Ma, Y.; Chen, Y. Preventing Graphene Sheets from Restacking for High-Capacitance Performance. *J. Phys. Chem. C* **2011**, *115*, 23192–23197.

(27) Cai, X.; Lai, L.; Shen, Z.; Lin, J. Graphene and Graphene-Based Composites as Li-Ion Battery Electrode Materials and their Application in Full. *J. Mater. Chem. A* **2017**, *5*, 15423–15446.

(28) Fu, H.; Xu, Z.; Guan, W.; Shen, X.; Cao, L.; Huang, J. Adsorption Contributions of Graphene to Sodium Ion Storage Performance. *J. Phys. D: Appl. Phys.* **2018**, *51*, 205501.

(29) Eom, W.; Park, H.; Noh, S. H.; Koh, K. H.; Lee, K.; Lee, W. J.; Han, T. H. Strengthening and Stiffening Graphene Oxide Fiber with Trivalent Metal Ion Binders. *Part. Part. Syst. Charact.* **2017**, *34*, 1600401.

(30) Jiao, X.; Qiu, Y.; Zhang, L.; Zhang, X. Comparison of the Characteristic Properties of Reduced Graphene Oxides Synthesized from Natural Graphites with Different Graphitization Degrees. *RSC Adv.* **2017**, *7*, 52337–52344.

(31) Rajamani, M.; Mishra, V. R.; Maliyekkal, S. M. Bundled-Firewood like AlOOH-CaCl<sub>2</sub> Nanocomposite Desiccant. *Chem. Eng. J.* **2017**, *323*, 171–179.

(32) Wang, S.; Zhang, X.; Feng, Z. C.; Cui, Y. Surface Chemical and Local Electronic Properties of Al<sub>x</sub>Ga<sub>1-x</sub>N Epi-Layers Grown by MOCVD. *Opt. Express* **2014**, *22*, 17440–17447.

(33) Gómez, D. A.; Coello, J.; MasPOCH, S. The Influence of Particle Size on the Intensity and Reproducibility of Raman Spectra of Compacted Samples. *Vib. Spectrosc.* **2019**, *100*, 48–56.

(34) Eom, W.; Kim, A.; Park, H.; Kim, H.; Han, T. H. Graphene-Mimicking 2D Porous Co<sub>3</sub>O<sub>4</sub> Nanofibers for Lithium Battery Applications. *Adv. Funct. Mater.* **2016**, *26*, 7605–7613.

(35) Noh, S. H.; Eom, W.; Lee, W. J.; Park, H.; Ambade, S. B.; Kim, S. O.; Han, T. H. Joule Heating-Induced sp<sup>2</sup>-Restoration in Graphene Fibers. *Carbon* **2019**, *142*, 230–237.

(36) Ryu, W.-H.; Yoon, T.-H.; Song, S. H.; Jeon, S.; Park, Y.-J.; Kim, I.-D. Bifunctional Composite Catalysts Using Co<sub>3</sub>O<sub>4</sub> Nanofibers Immobilized on Nonoxidized Graphene Nanoflakes for High-Capacity and Long-Cycle Li–O<sub>2</sub> Batteries. *Nano Lett.* **2013**, *13*, 4190–4197.

(37) Li, Z.; Chen, Y.; Jian, Z.; Jiang, H.; Razink, J. J.; Stickle, W. F.; Neufeind, J. C.; Ji, X. Defective Hard Carbon Anode for Na-Ion Batteries. *Chem. Mater.* **2018**, *30*, 4536–4542.

(38) Qin, J.; Kheimeh Sari, H. M.; He, C.; Li, X. A Hybrid Energy Storage Mechanism of Carbonous Anodes Harvesting Superior Rate Capability and Long Cycle Life for Sodium/Potassium Storage. *J. Mater. Chem. A* **2019**, *7*, 3673–3681.

(39) Nayak, P. K.; Yang, L.; Brehm, W.; Adelhelm, P. From Lithium-Ion to Sodium-Ion Batteries: Advantages, Challenges, and Surprises. *Angew. Chem., Int. Ed.* **2018**, *57*, 102–120.

(40) Delmas, C. Sodium and Sodium-Ion Batteries: 50 Years of Research. *Adv. Energy Mater.* **2018**, *8*, 1703137.

(41) Bommier, C.; Surta, T. W.; Dolgos, M.; Ji, X. New Mechanistic Insights on Na-Ion Storage in Nongraphitizable Carbon. *Nano Lett.* **2015**, *15*, 5888–5892.

(42) Qiu, S.; Xiao, L.; Sushko, M. L.; Han, K. S.; Shao, Y.; Yan, M.; Liang, X.; Mai, L.; Feng, J.; Cao, Y.; Ai, X.; Yang, H.; Liu, J. Manipulating Adsorption-Insertion Mechanisms in Nanostructured Carbon Materials for High-Efficiency Sodium Ion Storage. *Adv. Energy Mater.* **2017**, *7*, 1700403.

(43) Sun, N.; Guan, Z.; Liu, Y.; Cao, Y.; Zhu, Q.; Liu, H.; Wang, Z.; Zhang, P.; Xu, B. Extended “Adsorption–Insertion” Model: A New Insight into the Sodium Storage Mechanism of Hard Carbons. *Adv. Energy Mater.* **2019**, *9*, 1901351.

(44) Wang, Y.-X.; Chou, S.-L.; Liu, H.-K.; Dou, S.-X. Reduced Graphene Oxide with Superior Cycling Stability and Rate Capability for Sodium Storage. *Carbon* **2013**, *57*, 202–208.

(45) Hou, H.; Qiu, X.; Wei, W.; Zhang, Y.; Ji, X. Carbon Anode Materials for Advanced Sodium-Ion Batteries. *Adv. Energy Mater.* **2017**, *7*, 1602898.

(46) Park, K.; Yu, B.-C.; Goodenough, J. B. Li<sub>3</sub>N as a Cathode Additive for High-Energy-Density Lithium-Ion Batteries. *Adv. Energy Mater.* **2016**, *6*, 1502534.

(47) Matei Ghimbeu, C.; Górká, J.; Simone, V.; Simonin, L.; Martinet, S.; Vix-Guterl, C. Insights on the Na<sup>+</sup> Ion Storage Mechanism in Hard Carbon: Discrimination between the Porosity, Surface Functional Groups and Defects. *Nano Energy* **2018**, *44*, 327–335.

(48) Wang, Y.; Song, Y.; Xia, Y. Electrochemical Capacitors: Mechanism, Materials, Systems, Characterization and Applications. *Chem. Soc. Rev.* **2016**, *45*, 5925–5950.

(49) Chen, C.; Wang, Z.; Zhang, B.; Miao, L.; Cai, J.; Peng, L.; Huang, Y.; Jiang, J.; Huang, Y.; Zhang, L.; Xie, J. Nitrogen-Rich Hard Carbon as a Highly Durable Anode for High-Power Potassium-Ion Batteries. *Energy Storage Materials* **2017**, *8*, 161–168.

(50) Augustyn, V.; Simon, P.; Dunn, B. Pseudocapacitive Oxide Materials for High-Rate Electrochemical Energy Storage. *Energy Environ. Sci.* **2014**, *7*, 1597–1614.

(51) Rosenberg, F.; Ionescu, E.; Nicoloso, N.; Riedel, R. High-Temperature Raman Spectroscopy of Nano-Crystalline Carbon in Silicon Oxycarbide. *Materials* **2018**, *11*, 93.

(52) Kaushik, V. K.; Vijayalakshmi, R. P.; Choudary, N. V.; Bhat, S. G. T. XPS Studies on Cation Exchanged Zeolite A. *Microporous Mesoporous Mater.* **2002**, *51*, 139–144.

(53) Lu, W.; Iwasa, Y.; Ou, Y.; Jinno, D.; Kamiyama, S.; Petersen, P. M.; Ou, H. Effective Optimization of Surface Passivation on Porous Silicon Carbide using Atomic Layer Deposited Al<sub>2</sub>O<sub>3</sub>. *RSC Adv.* **2017**, *7*, 8090–8097.